

## Numerical and Experimental Study on Measurement of a Single Red Blood Cell Deformability Using a Microchannel and Electric Sensors

Ryouji FUJIWARA, Kazuya TATSUMI\*,  
Yoichi KATSUMOTO and Kazuyoshi NAKABE

Department of Mechanical Engineering and Science,  
Kyoto University, Kyoto 606-8501, Japan

\*corresponding author, E-mail: tatsumi@me.kyoto-u.ac.jp

### Abstract

An electric micro-resistance sensor that can continuously measure the deformability of a single red blood cell (RBC) in a microchannel and a numerical model that can simulate the resistance and capacitance of the cell membrane and cytoplasm are developed and improved. The resistance signal pattern between the electrodes is measured to evaluate the feasibility of the present sensor, using the human RBCs samples of normal RBCs and rigidized ones treated with  $\text{Ca}^{2+}$  and ionophore A23187. Synchronized with the resistance measurement, the behavior of the RBC is visualized using a high speed video camera. A correlation between the resistance signal pattern and the RBC deformation image is observed. Furthermore, in order to examine the influence of the sensor's parameters, especially the RBC height position and the sensor electrode arrangement, on the sensor sensitivity, numerical simulations are carried out for the harmonic electric field formed around a single RBC and the electrodes of the sensor in the microchannel. A numerical model introducing the equivalent electric circuit of the RBC successfully simulated the current density distributions by considering the potential drops produced by the resistance and capacitance of the membrane. The numerical results show that the variation of the RBC height position greatly influences the sensitivity and uncertainty of the sensor output signal. Rearrangement of the sensor electrode following these results, effectively suppresses the height influence and improves the sensor performance.

### 1. Introduction

Measurement of the red blood cell (RBC) deformability is an important issue from the viewpoint not only to clarify the hydrodynamic characteristics of the blood as fluid viscosity, but also to diagnose the initial symptoms of diseases during clinical investigation. For example, Plasmodium falciparum, a highly infectious parasite that causes severe anemia in a number of tissues and organs [1], considerably reduces the deformability of RBCs by producing cytoadherence-related neoantigens [2], [3]. Therefore, if a technique that can measure the deformability of these RBCs through a cheap, fast, simple and accurate procedure is de-

veloped, it would make a large contribution to the field of medicine, particularly in the area of clinical testing [4].

The microsensor proposed in this study evaluates the RBC deformability by measuring and analyzing the electric resistance of RBCs as they pass between a pair of electrodes embedded in the microchannel. Compared with the conventional optical measurements [5], [6], the present sensor offers the advantages of decreasing the size, cost and measuring time, and also showing greater compatibility with existing RBC counting equipment.

In this study, a microsensor consisting of microchannel and micro-electrodes was fabricated and the resistance measurement was made to demonstrate the feasibility of the present sensor. Samples of normal RBCs, and rigidified ones prepared by controlling the  $\text{Ca}^{2+}$  concentration in the cytoplasm with ionophore that was similar to those in vivo were used in the measurement.

The results were compared with the visualization results to determine the relation between the resistance distribution and the deformation rate of individual RBC, and to evaluate the performance of the proposed sensor. Additionally, numerical simulations were carried out to examine the effects of several parameters representing the sensor geometry on the sensor's sensitivity for the purpose of gaining insights that would ensure the design of an improved sensor.

In order to conduct accurate computations on the resistance distribution obtained as the RBCs passed between the electrodes, a new model that could simulate the resistance and capacitance of the cell membrane and cytoplasm was developed in this study. Attentions were particularly paid on the RBC height location and the sensor electrode arrangement that were considered to greatly influence the measurement sensitivity and uncertainty.

### 2. Measurement physics

Figure 1 illustrates the schematic of the measurement technique of this study. When the RBC flows through the high shear flow produced in the microchannel, it is stretched in the flow direction. If the applied shear stress is constant for each RBC, the deformation degree, in other words shape of the RBC, corresponds to the deformability of the RBC.

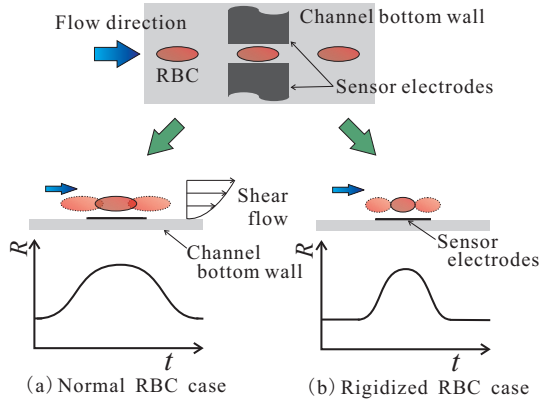


Figure 1: Concept of the present measurement system.

Table 1: Dimensions of the channel and electrodes (Experiment).

$W$ [ $\mu\text{m}$ ]	$W_r$ [ $\mu\text{m}$ ]	$H_1$ [ $\mu\text{m}$ ]	$H_2$ [ $\mu\text{m}$ ]
1000	50	52	10
$w_s$ [ $\mu\text{m}$ ]	$l_{sg}$ [ $\mu\text{m}$ ]	$l_s$ [ $\mu\text{m}$ ]	$l_g$ [ $\mu\text{m}$ ]
5.4	4.3	12.7	18.5

Therefore, the RBC deformability can be evaluated by measuring the deformation degree of the RBC accurately. In this study, we will employ the electric resistance measurement technique using a micro-resistance sensor of counter-type electrodes to evaluate the deformation degree of the RBC suspended in the microchannel flow.

The micro-resistance sensor is made of counter-type membrane electrodes that are attached to the bottom wall of the microchannel. The electric resistance between these sensor electrodes is continuously monitored as each RBC passes between the electrodes. Since the RBC membrane has the electric conductivity of approximately  $1 \times 10^{-6} \text{S/m}$  that is much smaller than those of cytoplasm  $1.67 \text{S/m}$  and solvents, the RBC membranes can be regarded as electric insulators in the electric field. Therefore, the measured resistance increases only while a RBC passes between the electrodes. Since the membrane is the major factor that influences the electric resistance, the value and distribution of the resistance will vary depending on the shape of the RBC as shown in Fig. 1(a) and (b). This characteristic of resistance is used to evaluate the deformation degree in this study.

### 3. Experiment

Before discussing the numerical procedure and results of this study, the results of the measurement using the micro-sensor developed by the authors group are described in this section to provide some information on the measurement technology.

#### 3.1. Microchannel and electrodes geometry

Figure 2 illustrates the schematic view of the microchannel and electrodes of micro-sensor. The dimensions of each

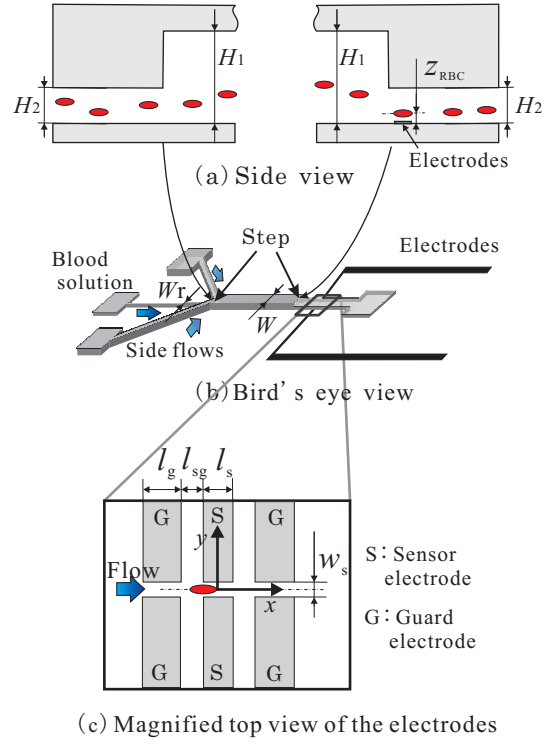


Figure 2: Schematic of RBC-detecting microchannel.

value are specified in Table 1. The microchannel is made from polydimethylsiloxane (PDMS) and is bonded with a slide-glass. Platinum counter-type electrodes are attached to the bottom wall. This channel has three inlets as shown in Fig. 2(b); central-flow inlet and two side-flow inlets. RBC suspension is supplied from the central-flow inlet. The two side-flows produce a sheath flow that can control the span-wise positions of RBCs precisely by independently controlling the flow rate of side-flows. Further, backward-facing and forward-facing steps are installed in the microchannel (cf. Fig. 2(a)) in order to control the height position of RBC to be located close to the electrodes. This will enhance the sensitivity of the sensor because a high current density of the electric field is obtained in the area close to the electrodes.

As shown in Fig. 2(c), the electrodes are placed perpendicular to the flow. These electrodes consist of the sensor and guard electrodes. The sensor electrodes used to measure the resistance are placed in the middle. The electrodes located at both sides of the sensor electrodes are guard electrodes to which electric potential equal to the sensor electrodes is applied for the purpose of reducing the fringe effect of the electric field. Platinum black coating is applied on all the electrodes to reduce the potential drop due to the electric double layer formed on the electrode surfaces.

#### 3.2. Experimental procedure and conditions

RBC solution and solvent are supplied to central-flow inlet and side-flow ones of the microchannel using syringes and syringe pumps (Harvard Apparatus Co.; econoflo,

Nihon-Kohden Co.; CFV-3200) with flow rates of 0.02 and  $1.0\mu\text{L}/\text{min}$ , respectively. The complex impedance between the sensor electrodes is measured as the RBC passes between them at 10kHz AC frequency, and the resistance is derived from the real part of this complex impedance.

Synchronized with the resistance measurement, the behavior of the RBC is visualized using a microscope (OLYMPUS Co.; IX-71),  $\times 100$  objective lens (OLYMPUS Co.; LMPLFLN100X), and a high speed video camera (Vision Research; Phantom V7.3). Flame rate and exposure time of the camera are 1000fps and  $99\mu\text{s}$ , respectively. The spatial resolution and the focal depth of the video images are  $0.21\mu\text{m}/\text{pixel}$  and  $1.7\mu\text{m}$ , respectively. Detail information on the apparatus and measurement method are described in the authors' previous publication [7].

The deformation degree of the RBC is evaluated with the video images to be compared with the resistance distribution. The deformation degree of the RBC is presented by the deformation index,  $DI$  as defined by Eq. (1) [6].  $a$  and  $b$  are the RBC's lengths in  $x$  and  $y$  directions, respectively.

$$DI = \frac{a - b}{a + b} \quad (1)$$

Small amount of sample blood is collected from a single healthy human donor (one of the present authors). In order to obtain RBCs with different deformability, three types of RBCs are prepared in the experiment. The first one is referred to as normal RBCs: The RBCs are separated from other suspended materials by centrifugation (1000G) for 10 minutes. After removing the supernatant liquid, the deposit is suspended to 0.5mL phosphate buffered saline (PBS) to which 10wt% polyvinylpyrrolidone (PVP) is added. The second sample is referred to as rigidized RBCs [8]: RBCs are separated by centrifugation (1000G) for 10 minutes. After removing the supernatant, the rest is suspended to buffer solution of A23187 ionophore ( $1\mu\text{mol}/\text{L}$  A23187,  $1\mu\text{mol}/\text{L}$   $\text{CaCl}_2$ ,  $10\text{mmol}/\text{L}$   $\text{KCl}$ ,  $130\text{mmol}/\text{L}$   $\text{NaCl}$ ,  $2\text{mmol}/\text{L}$   $\text{MgCl}_2$ ,  $15\text{mmol}/\text{L}$  tris,  $\text{pH}=7.4$ ). The buffer solution with RBCs is incubated at  $37^\circ\text{C}$  for 40 minutes. Then, the solution is centrifuged (1000G) for 10 minutes, and RBCs are suspended to 0.5mL PBS with 10wt% PVP. The third RBC sample is the spherocyte: RBCs are separated by centrifugation (1000G) for 10 minutes, and are suspended in buffer solution of A23187 ionophore ( $1\mu\text{mol}/\text{L}$  A23187,  $2\mu\text{mol}/\text{L}$   $\text{CaCl}_2$ ,  $10\text{mmol}/\text{L}$   $\text{KCl}$ ,  $130\text{mmol}/\text{L}$   $\text{NaCl}$ ,  $2\text{mmol}/\text{L}$   $\text{MgCl}_2$ ,  $15\text{mmol}/\text{L}$  tris,  $\text{pH}=7.4$ ). This solution is incubated at  $37^\circ\text{C}$  for 40 minutes. Then the RBCs are centrifuged (1000G) for 10 minutes, and are suspended to 0.5mL PBS with 10wt% PVP.

It should be noted here that PVP is added to the solutions in order to increase the fluid viscosity. This increases the flow shear stress applied to the RBC under the same flow rate condition, and increases the deformation degree of the RBC. The viscosity of the solution measured by the rheometer is  $1.84 \times 10^{-1}\text{Pa}\cdot\text{s}$ .

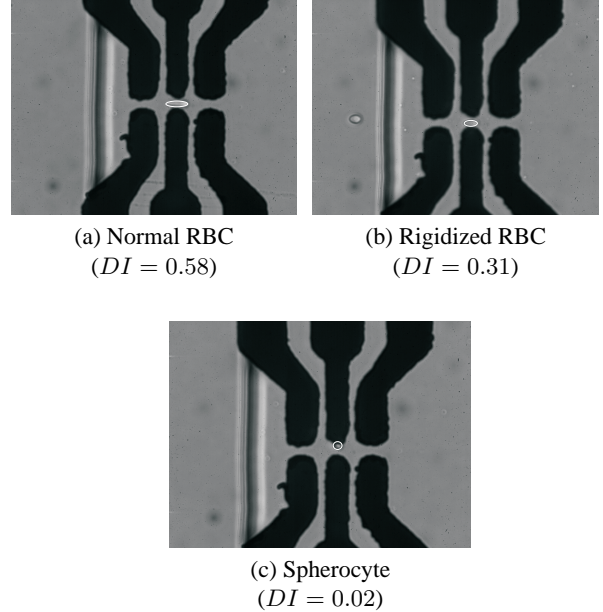


Figure 3: Photographs of RBC with various  $DI$  passing between the electrodes.

Table 2: Average values of the size and shape parameters.

	Samples	$\bar{a}$ [ $\mu\text{m}$ ]	$\bar{b}$ [ $\mu\text{m}$ ]	$\overline{DI}$
Normal RBC	57	13.93	3.86	0.56
Rigidized RBC	30	13.72	4.66	0.48
Spherocyte	8	5.00	4.81	0.02

### 3.3. Visualization results of RBCs

Figure 3 shows the photographs of the RBCs at time  $t = 0$  that is the moment the RBC passes the center of the sensor electrodes. The photographs (a), (b) and (c) show the results of the normal RBC ( $DI = 0.58$ ), rigidized RBC ( $DI = 0.31$ ), and spherocyte ( $DI = 0.02$ ), respectively. As shown in Fig. 3(a), the normal RBC is stretched in the streamwise direction due to the shear stress of the flow. The rigidized RBC shown in Fig. 3(b) is also deformed in  $x$ -direction similar to normal RBC, however, the deformation degree is relatively smaller. Therefore, it is confirmed that the deformability of the rigidized RBC is decreased by the rigidizing treatment. As for the spherocyte shown in Fig. 3(c), the RBC keeps its spherical shape in spite of the applied shear stress.

The average deformability index,  $\overline{DI}$ , measured from the images is shown in Table 2 together with the average values of  $\bar{a}$ ,  $\bar{b}$ , and the sample number.

### 3.4. Electric resistance measurement

Figure 4 shows the distribution of the resistance variation,  $\Delta R_x$ , as the RBC passes between the electrodes in the cases of the typical results of the normal RBC, rigidized RBC and spherocyte. Note that the data is smoothed for analysis by averaging adjacent 15 points.  $\Delta R_x$  is defined as Eq. (2),

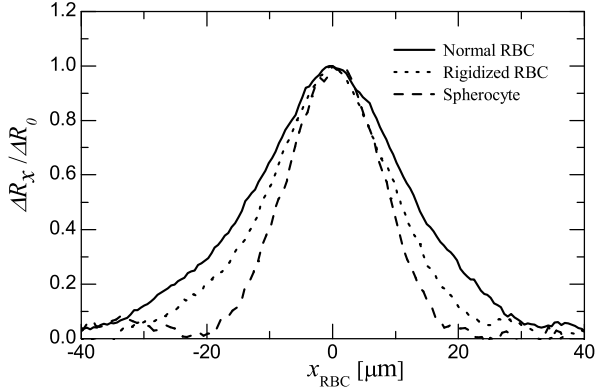


Figure 4: Relationship between the normalized resistance variation and RBC streamwise position.

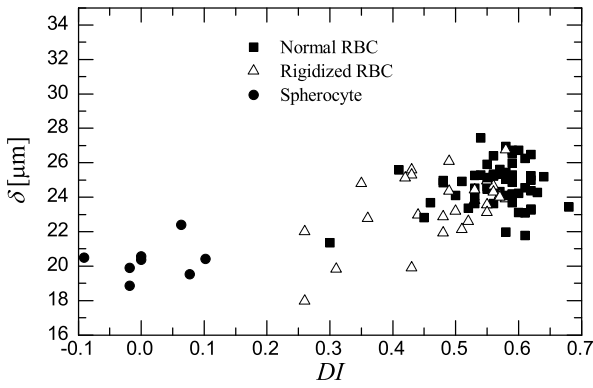


Figure 5: Relation between  $\delta$  and  $DI$ .

Table 3: Average half-width  $\bar{\delta}$  for each type of RBC.

	Samples	$\bar{\delta}[\mu\text{m}]$
Normal RBC	57	26.25
Rigidized RBC	30	24.74
Spherocyte	8	20.30

where  $R(x_{\text{RBC}})$  and  $R(\infty)$  are the resistances measured at the moment when the RBC is located at  $x_{\text{RBC}}$  and infinitely far from the electrodes, respectively.  $x_{\text{RBC}}$  is the streamwise position of the center of RBC and  $\Delta R_0$  is  $\Delta R_x$  of  $x_{\text{RBC}} = 0$ .

$$\Delta R_x = R(x_{\text{RBC}}) - R(\infty) \quad (2)$$

Figure 4 shows the typical resistance distribution of each type of RBC. The bottom width of each peak is longer in the order of, normal RBC, rigidized RBC and spherocyte. Next, by analyzing the resistance distributions and comparing them with the visualization results, the relation between the half-width of the  $\Delta R_x$  peak height,  $\delta$ , and  $DI$  for every sample are obtained and plotted in Fig. 5. Further, the average half-width  $\bar{\delta}$  of each type of RBC is shown in Table 3. The electric current flows from one side to the other side of the sensor electrodes. When a RBC interrupts this current

flow the electric resistance will increase. Considering then that a RBC with larger  $DI$  has a longer streamwise length  $a$ , the RBC will start to interrupt the current flow at a streamwise position located further upstream compared with the RBC with smaller  $DI$ . As a result, the width of the resistance distribution increases as  $DI$  increases. As one can see in the figure and table, positive correlation between  $\delta$  and  $DI$  is observed;  $DI$  becomes larger as  $\delta$  increases. These results show that the deformation degree can be measured by measuring the resistance distribution, and the feasibility of this sensor is confirmed.

However, Figure 5 also shows relatively large variation in the  $\delta$  distribution for each  $DI$ . One of the reasons of this uncertainty is that the current density distribution is dense in the area adjacent to the bottom wall and gradually decreases in the height direction. Even if RBCs passing between the sensor electrodes have the same  $DI$ , the amount of the current density interrupted by each RBC can change when the RBC height position varies. It has been found in experiments that the variation of the RBC height position is approximately  $1.7\mu\text{m}$ , and can influence the resistance distributions. Other reasons for the data uncertainty are: the difference of individual RBC size with the same  $DI$ , the variation of the RBC spanwise position and S/N ratio of the resistance measurement. Among these influences, the RBC height position and the electrode arrangement will be discussed further in Section 4.

## 4. Numerical simulation

As mentioned in Section 3.4, relatively large variation of  $\delta$  in each  $DI$  is considered to be attributed particularly to the RBC height position and S/N ratio of the resistance measurement. It is, however, difficult to precisely evaluate the influences of these factors, and to suggest the improved design of the micro-sensor experimentally. It is, therefore, important to develop a numerical model that can simulate the resistance measured by the electrodes as the RBC passes between them. In the following sections, the numerical model will be examined, and the results evaluating the influences of the RBC shape, RBC height position, and the electrode arrangement on the resistance distribution will be discussed.

### 4.1. Numerical procedure and RBC model

Three-dimensional finite element method (3D-FEM) simulation is carried out for the harmonic electric field formed around the RBC and the electrodes placed in the microchannel using a commercially available 3D-FEM software COMSOL (COMSOL Multiphysics Co.). In the simulation, the governing equation shown in Eq. (3) is solved, where  $V$  is the electric potential.  $\epsilon'$  and  $\kappa$  are relative permittivity and electric conductivity, respectively.  $\epsilon_0$  is the vacuum permittivity, and  $f$  is the frequency of the supplied potential.

$$\nabla \cdot \left( (\epsilon' - i \frac{\kappa}{2\pi f \epsilon_0}) \nabla V \right) = 0 \quad (3)$$

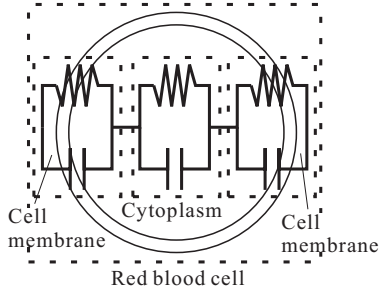


Figure 6: Equivalent circuit model for an RBC.

Table 4: Each parameter of RBC, PBS, Glass and PDMS.

$\epsilon'_{cp}$	$\kappa_{cp}[\text{S/m}]$	$\epsilon'_{cm}$	$\kappa_{cm}[\text{S/m}]$
50	0.67	5	$1 \times 10^{-7}$
$t_{cm}[\text{nm}]$	$d_{\text{RBC}}[\mu\text{m}]$	$\epsilon'_{\text{PBS}}$	$\kappa_{\text{PBS}}[\text{S/m}]$
5	6.7	78.3	1.67
$\epsilon'_{\text{Glass}}$	$\kappa_{\text{Glass}}[\text{S/m}]$	$\epsilon'_{\text{PDMS}}$	$\kappa_{\text{PDMS}}[\text{S/m}]$
3.4	$1 \times 10^{-12}$	2.5	$1 \times 10^{-12}$

The complex impedance  $Z^*$  that would be measured by the sensor electrodes, is obtained from the complex electric current passing through the electrode surfaces. The equivalent circuit of the RBC that consists of the cell membrane and cytoplasm can be described as a parallel circuit of resistor and capacitor as shown in Fig. 6. Katsumoto [9] suggested a model that considered the cell as a sphere with uniform complex relative permittivity  $\epsilon_{\text{RBC}}^*$ .  $\epsilon_{\text{RBC}}^*$  was defined as Eq. (4) derived by Hanai using the relative permittivities of the cell membrane  $\epsilon_{\text{cm}}^*$  and cytoplasm  $\epsilon_{\text{cp}}^*$ .

$$\epsilon_{\text{RBC}}^* = \epsilon_{\text{cm}}^* \frac{2(1-\nu)\epsilon_{\text{cm}}^* + (1+2\nu)\epsilon_{\text{cp}}^*}{(2+\nu)\epsilon_{\text{cm}}^* + (1-\nu)\epsilon_{\text{cp}}^*} \quad (4)$$

$$\nu = \left( \frac{d_{\text{RBC}} - 2t_{\text{cm}}}{d_{\text{RBC}}} \right)^3 \quad (5)$$

$d_{\text{RBC}}$  and  $t_{\text{cm}}$  are the diameter of the RBC and the membrane thickness, respectively. The complex relative permittivity  $\epsilon^*$  is defined as Eq. (6) in terms of the relative permittivity  $\epsilon'$  and the electrical conductivity  $\kappa$ . Table 4 indicates relevant physical properties.

$$\epsilon^* \equiv \epsilon' - i \frac{\kappa}{2\pi f \epsilon_0} \quad (6)$$

This model has shown a good performance and a marked reduction of computational load by decreasing the grid number. This model is, however, limited only to spherical cells and is not fully applicable for the present computation that should evaluate the influences of the RBC shape (deformation degree) on the electric field. In order to tackle this problem, the following model is proposed in this study.

As mentioned previously, the RBC consists of cytoplasm and membrane. The thickness of the membrane is

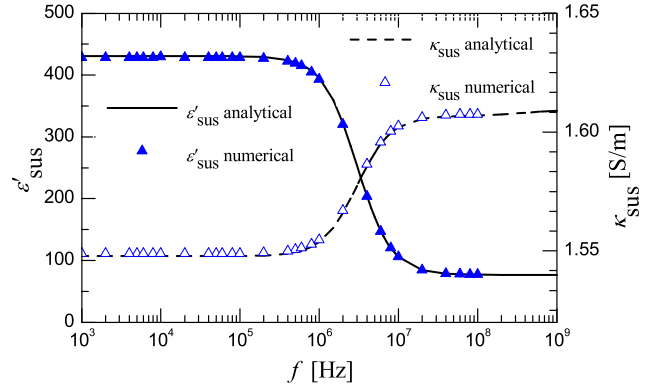


Figure 7:  $\epsilon_{\text{sus}}^*(f)$  of spherical RBCs suspended in PBS.

much smaller than the diameter of the cytoplasm, and directly solving this part in the computation is extremely difficult. Instead of using the composite complex permittivity represented in Eq. (4), the boundary condition at the surface of the RBC is modified in the new model. In this case, the potential drop produced by the resistance and capacitance of the membrane is considered as Eq. (7) and applied to the boundary between the cell and fluid.

$$\vec{j} \cdot \vec{n} = \frac{(\kappa_{\text{cm}} + i2\pi f \epsilon_0 \epsilon'_{\text{cm}})(V_{\text{out}} - V_{\text{in}})}{t_{\text{cm}}} \quad (7)$$

$\vec{j}$  [A/m<sup>2</sup>] is a current density that passes through the cell boundary.  $\vec{n}$  is a unit normal vector of the RBC surface.  $V_{\text{out}}$  [V] and  $V_{\text{in}}$  [V] are, respectively, the voltages at the apparent boundaries between the membrane and fluid, and between the membrane and cytoplasm. Obviously, this boundary condition can be applied to the membranes of RBCs with arbitrary shapes, and is effective for the present computation.

## 4.2. Validation of the numerical model

In order to validate the model, the frequency dependence of relative permittivity  $\epsilon'_{\text{sus}}$  and conductivity  $\kappa_{\text{sus}}$  of a domain filled with solvent is examined in the case that a single RBC is suspended. The domain is a cubic with the length of 14.7  $\mu\text{m}$ , and the volume fraction of the RBC is 0.05.

The results are compared with analytical ones obtained from Eq. (4), and are shown in Fig. 7. In the figure, the results obtained by the present model excellently correspond with the analytical ones. This assures the validity of the model. Further, conductivity of the suspension  $\kappa_{\text{sus}}$  sharply increases approximately at  $f = 10^6$  Hz showing the relaxation for high frequency AC electric field. This indicates that the RBC membrane acts as an insulating film in the range of relatively low frequency below 100 kHz, and the measuring frequency should be kept below this value in order to detect the resistance variation caused by the RBC passing.

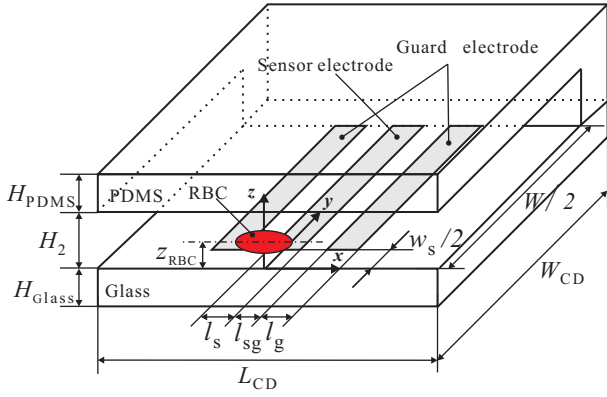


Figure 8: Computational domain of counter-type electrodes.

Table 5: Dimensions of the computational domain.

$L_{CD}$ [ $\mu\text{m}$ ]	$W_{CD}$ [ $\mu\text{m}$ ]	$W$ [ $\mu\text{m}$ ]	$H_{PDMS}$ [ $\mu\text{m}$ ]
800	700	1000	100
$H_{Glass}$ [ $\mu\text{m}$ ]	$H_2$ [ $\mu\text{m}$ ]	$l_s$ [ $\mu\text{m}$ ]	$l_g$ [ $\mu\text{m}$ ]
100	10	12	20
$l_{sg}$ [ $\mu\text{m}$ ]	$w_s$ [ $\mu\text{m}$ ]		
4	6		

Table 6: Values of size and shape parameter.

	$a$ [ $\mu\text{m}$ ]	$b$ [ $\mu\text{m}$ ]	$DI$
Ellipsoidal shape	14	4	0.55
Spherical shape	6.7	6.7	0.00

### 4.3. The influence of the RBC height position on the resistance distribution

Numerical simulations on the resistance measurement using the present sensor will be conducted now. As discussed in Section 3.4, the measurement variation against each  $DI$  is relatively large, and the sensitivity of the half-width  $\delta$  for  $DI$  is small. It is, therefore, required to improve the sensitivity of the present sensor considering the practical use in the medical field. The major factors that influence the sensitivity and measurement variation are believed to be the height position of the RBC, and electrode width and arrangement. Among these parameters, the effects of the RBC height position  $z_{RBC}$  and the electrode arrangement will be discussed in the present computation.

The computational domain is shown in Fig. 8 with the coordinates and parameters. The dimensions are tabulated in Table 5. The domain includes the channel top wall made of PDMS and the bottom wall made of glass. Relative permittivity  $\epsilon'_{cp}$  and conductivity  $\kappa_{cp}$  of the RBC, PDMS, and glass employed in the computation are listed in Table 4. The electrode thickness is set as zero. Symmetric boundary conditions are applied in the  $x$ - $z$  plane at  $y = 0$ , and 0V conditions are applied to the streamwise boundaries. 0.5V is applied to the surface of the electrodes with a frequency

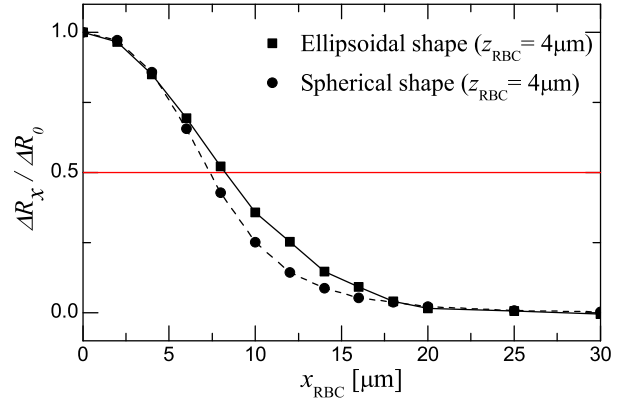


Figure 9: Normalized resistance distributions of the RBC streamwise position (RBC shape effect).

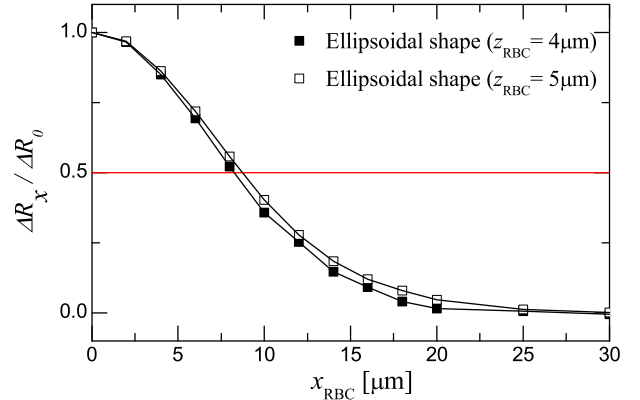


Figure 10: Normalized resistance distributions of the RBC streamwise position (height effect in ellipsoidal RBC case).

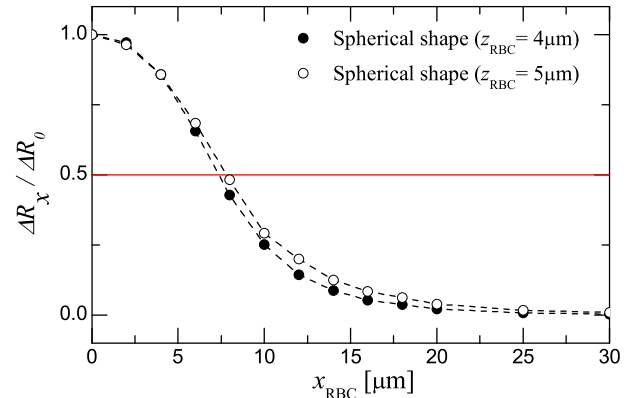


Figure 11: Normalized resistance distributions of the RBC streamwise position (height effect in spherical RBC case).

Table 7:  $z_{RBC}$  and RBC shape effects on  $\delta$  and  $\Delta R_0$ .

$z_{RBC}$ [ $\mu\text{m}$ ]	$\delta$	
	Ellipsoidal shape [ $\mu\text{m}$ ]	Spherical shape [ $\mu\text{m}$ ]
4.0	16.5	14.7
5.0	17.5	15.6
$z_{RBC}$ [ $\mu\text{m}$ ]	$\Delta R_0$	
	Ellipsoidal shape [ $\Omega$ ]	Spherical shape [ $\Omega$ ]
4.0	$4.46 \times 10^3$	$6.64 \times 10^3$
5.0	$3.93 \times 10^3$	$4.86 \times 10^3$

of 10kHz. In order to obtain the complex admittance and the resistances of the region located between the opposite-facing sensor electrodes, complex currents distributed on the surface of the sensor electrode are integrated and divided by the applied voltage 1V.

The streamwise position of the RBC is varied fixing the spanwise position at  $y = 0$  to simulate the resistance distribution as the RBC passes the electrodes. Two different RBC shapes, ellipsoid and sphere, are considered in the computation in order to discuss the influence of the RBC deformation degree on the resistance distribution. In this case, the RBC shape is changed keeping the surface area of the RBC constant. The streamwise and spanwise lengths  $a$  and  $b$ , and the  $DI$  of these RBCs are shown in Table 6.

The influence of the RBC shape on the resistance distribution is first discussed here setting the height positions of both RBC shapes as  $z_{\text{RBC}} = 4\mu\text{m}$ . Figure 9 shows the  $\Delta R_x/\Delta R_0$  distributions against the streamwise position of the RBC,  $x_{\text{RBC}}$ . The distribution shows that the ellipsoidal RBC produces a wider distribution and half-width  $\delta$  of the distribution is greater than the one observed in the spherical RBC case. This trend corresponds well with the experiment shown in Fig. 4.

Next, the influence of the RBC height position  $z_{\text{RBC}}$  on the resistance distribution is discussed. Figures 10 and 11 show the relationship between the  $\Delta R_x/\Delta R_0$  and  $x_{\text{RBC}}$  in the cases of ellipsoidal and spherical RBCs. Table 7 shows the half-width  $\delta$  of the  $\Delta R_x/\Delta R_0$  distribution and  $\Delta R_0$  that presents the maximum value of  $\Delta R_x$ . It should be noted that the height  $z_{\text{RBC}} = 5\mu\text{m}$  is considered in this computation on basis of the fact that the variation of  $z_{\text{RBC}}$  was approximately  $\pm 0.85\mu\text{m}$  in the experiment.

As shown in Table 7, the maximum value  $\Delta R_0$  increases as  $z_{\text{RBC}}$  decreases. As mentioned previously, the current density distribution of the region located between the electrodes increases with a decrease in  $z_{\text{RBC}}$  which is correlated with the distance of the RBC center from the sensor surface. Therefore, in the case of smaller  $z_{\text{RBC}}$ , the RBC will pass close to the sensor electrodes in the area of much higher current density distribution leading to a greater value of the measured resistance. The  $\Delta R_x/\Delta R_0$  distributions shown in Figs. 10 and 11, differ comparing the cases of  $z_{\text{RBC}} = 4$  and  $5\mu\text{m}$ . The decrease of  $\Delta R_x$  depending on  $z_{\text{RBC}}$  will decrease the S/N ratio of the measured signal and deteriorate the sensor sensitivity. This results in the variation in the half-width  $\delta$  as shown in Table 7. The variation of  $\delta$  due to the change of the RBC height position will be comparable with the difference of  $\delta$  caused by the change in the RBC shape ( $= DI$ ) shown in Fig. 9. Thus, the variation of the RBC height position can greatly influence the measurement sensitivity and uncertainty.

#### 4.4. Electrode arrangement to increase the sensor sensitivity

As shown in the previous section, it was found that the RBC height position  $z_{\text{RBC}}$  influences the sensor sensitivity. One of the solutions to tackle this problem is to change the elec-

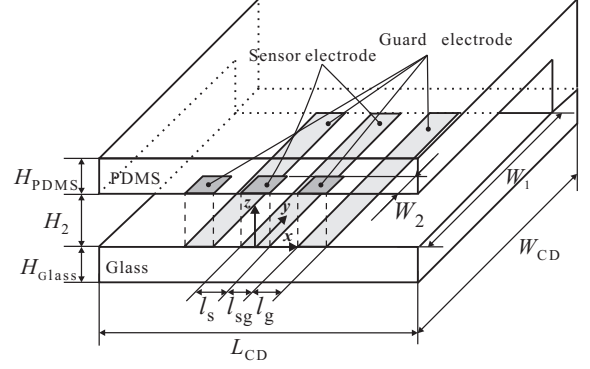


Figure 12: Computational domain of the cross-over type electrodes.

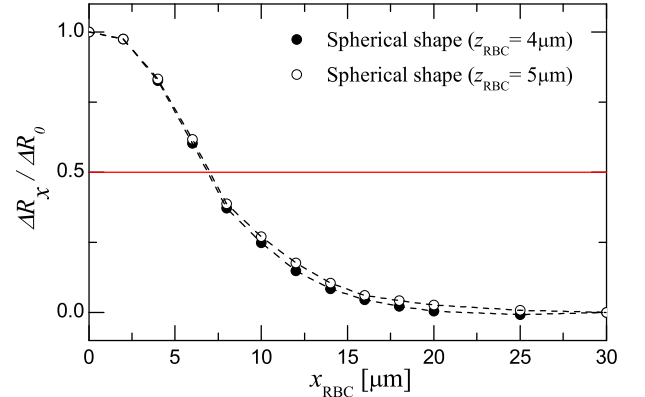


Figure 13: Normalized resistance distributions of the RBC streamwise position (height effect in spherical RBC case).

Table 8: Numerical result of the cross-over type sensor.

$z_{\text{RBC}} [\mu\text{m}]$	$\delta [\mu\text{m}]$	$\Delta R_0 [\Omega]$
4.0	13.9	$7.55 \times 10^3$
5.0	14.0	$7.32 \times 10^3$

trode width and increase the S/N ratio of the measurement. Another solution is to change the electrode arrangement that will be discussed in this section.

Figure 12 shows the electrode arrangement considered in this study. The electrodes are attached to the channel top and bottom walls to form an electric field mainly along the  $z$ -axis in the area between the electrodes. The current density in the area becomes relatively uniform in the height direction which indicates that the measured resistance is less influenced by  $z_{\text{RBC}}$ . It should be noted that it is important to carefully design the overlapping area of the upper and lower electrodes. If the area becomes too larger than the size of the RBC, the resistance variation  $\Delta R_x$  decreases. On the other hand, if the area becomes too small, it will be difficult to control the spanwise position of the RBC.

To evaluate the suggested electrode arrangement, the numerical computation on the domain shown in Fig. 12 is carried out. The additional dimensions of the domain are specified in the following;  $W_1 = 497\mu\text{m}$ ,  $W_2 = 5\mu\text{m}$ . Other dimensions of channel and electrodes are the same as Fig.

8. The boundary conditions and computational methods are also the same as those shown in Section 4.3.

Figure 13 shows the normalized resistance  $\Delta R_x/\Delta R_0$  distributions in the case of the spherical RBC. Table 8 shows  $\delta$  and  $\Delta R_0$  values. The results of  $z_{\text{RBC}} = 4$  and  $5\mu\text{m}$  are shown in the figure and table. The results shown in Fig. 13 indicate that the influence of  $z_{\text{RBC}}$  on the  $\Delta R_x/\Delta R_0$  distribution is much smaller compared with the case of the electrodes attached to the channel bottom wall. Actually, the half-width  $\delta$  of both cases shown by the line in the figure are almost identical. Further, the  $\Delta R_0$  values show greater values compared with those shown in Table 7. These results show that the sensor sensitivity and accuracy can be markedly improved by attaching the electrodes to the top and bottom walls providing a more uniform current density distribution.

## 5. Conclusions

An electric micro-resistance sensor that could measure the deformability of RBC in a microchannel was fabricated and the feasibility of micro-sensor was evaluated using normal, rigidized RBCs and spherocytes. Further, a numerical model that considers the resistor and capacitor of the cell membrane as boundary specific conditions was developed. Using this model, the influences of the RBC height position and sensor electrode arrangement were discussed. The major results are as follows:

- Rigidized RBCs and spherocytes could be prepared using  $\text{Ca}^{2+}$  and A23187.
- A correlation between the half-width  $\delta$  of the measured resistance distribution and the deformability index  $DI$  of RBC was observed. The feasibility of the present sensor was confirmed from these measurements.
- The proposed numerical model introducing the equivalent electric circuit of the RBC by considering the potential drops produced by the resistance and capacitance of the membrane was validated comparing the results of electric characteristics of a suspended RBC with the analytical ones.
- The variation of  $\delta$  due to the RBC height position was comparable with the difference of  $\delta$  by changing the RBC shape. The results showed that one of the reasons was attributed to the fact that both of the sensor electrodes were attached to the bottom wall. This electrode arrangement resulted in the decay of the electric field in the height direction. The uniform electric field which was formed by a new arrangement of electrodes attached to the top and bottom wall decreased the variation of  $\delta$  and improved the sensor sensitivity.

## Acknowledgement

This work was financially supported by the Ministry of Education, Culture, Sports and Science and Technology of Japan.

## References

- [1] L.H. Miller, D.I. Baruch, K. Marsh, O.K. Doumbo, The Pathogenic Basis of Malaria, *Nature* 415: 673-679, 2002.
- [2] A.M. Dondorp, P.A. Kager, J. Vreeken, N.J. White, Abnormal Blood Flow and Red Blood Cell Deformability in Severe Malaria, *Parasitology Today* 16: 228-232, 2000.
- [3] S. Suresh, J. Spatz, J.P. Mills, A. Micoulet, M. Dao, C.T. Lim, M. Beil, T. Seufferlein, Connections between Single-cell Biomechanics and Human Disease States: Gastrointestinal Cancer and Malaria, *Acta Biomaterialia* 1: 15-30, 2005.
- [4] C.T. Lim, E.H. Zhou, S.T. Quek, Mechanical Models for Living Cells - a Review, *Journal of Biomechanics* 39: 195-216, 2006.
- [5] M.C. Tracey, R.S. Greenaway, A. Das, P.H. Kaye, A.J. Barnes, A Silicon Micromachined Device for Use in Blood Cell Deformability Studies, *IEEE Biomedical Engineering* 42: 751-761, 1995.
- [6] N. Korin, A. Bransky, U. Dinnar, Theoretical Model and Experimental Study of Red Blood Cell (RBC) Deformation in Micro-channels, *Journal of Biomechanics* 40: 2088-2095, 2007.
- [7] Y. Katsumoto, K. Tatsumi, T. Doi, K. Nakabe, Electrical Classification of Single Red Blood Cell Deformability in High-shear Microchannel Flows, *International Journal of Heat and Fluid Flow* 31: 985-995, 2010.
- [8] T. Shiga, M. Sekiya, N. Maeda, K. Kon, M. Okazaki, Cell Age-dependent Changes in Deformability and Calcium Accumulation of Human Erythrocytes, *Biochimica et Biophysica Acta* 814: 289-299, 1985.
- [9] Y. Katsumoto, Y. Hayashi, I. Oshige, S. Omori, N. Kishii, A. Yasuda, K. Asami, Dielectric Cytometry with Three-dimensional Cellular Modeling, *Biophysical Journal* 95 (6): 3043-3047, 2008.